International Journal of Applied Earth Observation and Geoinformation 133 (2024) 104095

Contents lists available at ScienceDirect

International Journal of Applied Earth Observation and Geoinformation

journal homepage: www.elsevier.com/locate/jag

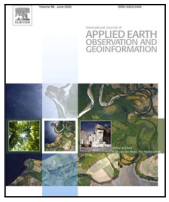

On the joint use of SAR and meteo-climatological information to monitor the Po River under nominal and drought conditions

Emanuele Ferrentino [a,*], Marco Polcari [a], Francesca Silverii [a], Christian Bignami [a], Ferdinando Nunziata [b], Salvatore Stramondo [a], Maurizio Migliaccio [a,b]

[a] Istituto Nazionale di Geofisica e Vulcanologia, Via di Vigna Murata, 605, Roma, 00143, Italy
[b] Università degli Studi di Napoli Parthenope, Centro Direzionale isola C4, Napoli, 80143, Italy

ARTICLE INFO

Keywords:
SAR
InSAR
Water body
Po River
Ground deformation
Sentinel-1

ABSTRACT

This study addresses the drought phenomenon that affected the Po River, north of Italy, by jointly exploiting methods based on measurements remotely sensed by the European Sentinel-1 C-band Synthetic Aperture Radar (SAR) and meteo-climatological information derived from both in situ and satellite datasets. The SAR methods consist of a baseline approach, which estimates the water-covered area from dual-polarized SAR imagery using a constant false alarm rate (CFAR) approach, augmented with ancillary vertical ground displacement information derived from SAR interferometry (InSAR). The meteo-climatological information includes hydrometric water level, rainfall data, and the Standard Precipitation Evapotranspiration Index (SPEI). Experimental results, obtained using a seven-year time series of SAR scenes collected over the Po River close to the city of Piacenza and contrasted with ancillary external information, demonstrate the soundness of the proposed SAR-based added-value products and their satisfactory accuracy in emphasizing both seasonal trends and the drought phenomena occurred in the area. This paves the way for an operational use of SAR measurements to monitor the water-covered area of the Po River and potentially other similar environments.

1. Introduction

Drought is a natural disaster with far-reaching consequences that have plagued civilizations for centuries, leaving an indelible mark on our world's social, economic, and environmental fabric. Water scarcity poses immense challenges for agriculture, ecosystems, and human well-being, demanding immediate attention and comprehensive solutions. Since 2003, there has been an increase in the frequency of drought events in the Po River Basin, the longest Italian river, leading to a gradual transformation in drought management (Musolino et al., 2018). In 2022, the Po River was affected by the most severe drought of the last 70 years, (Po River District Basin Authority - https://www.adbpo.it/ (Montanari et al., 2023; Clifford, 2022). At the beginning of 2022, a severe meteorological drought occurred over a large part of Europe causing an exceptional scarcity of precipitation in Northern Italy, and contributing to a prolonged hydrological drought that threatened water resources security in the area (Montanari et al., 2023). The continuous monitoring of the river basin is a key need to assist the planning and development of regional and/or national strategies for managing water resources. Satellite-based remote sensing platforms, due to their synoptic and non-cooperative observations at fine-to-moderate spatial resolution, can be exploited to improve the understanding and management of drought events. Optical sensors are a straightforward choice since their measurements are relatively simple to be interpreted. However, optical radiation is sunlight-dependent and severely affected by cloud cover and other adverse meteorological conditions that may limit the information extraction process, especially for monitoring purposes. These issues can be overcome by radar sensors that guarantee all-day and almost all-weather observations together with a wide area coverage. Among the radar sensors, the Synthetic Aperture Radar (SAR), due to its fine spatial resolution imaging capabilities (3 m to 30 m), is the key candidate for monitoring the time evolution of the water content of the Po River.

State-of-the-art SAR approaches to monitor the water extent of inland water basins are mainly based on the use of time series measurements. In Pipitone et al. (2018) visual matching and unsupervised classification approaches are used to analyze the water level of the Castello dam of the Magazzolo reservoir, Italy. Results, obtained using both X-band SAR and optical imagery show that the combination of different sensors can improve land/water discrimination. In Ding and Li (2011), a time series of Environmental Satellite (ENVISAT)

* Corresponding author.
E-mail address: emanuele.ferrentino@ingv.it (E. Ferrentino).

https://doi.org/10.1016/j.jag.2024.104095
Received 30 October 2023; Received in revised form 5 August 2024; Accepted 10 August 2024
Available online 19 August 2024

Advanced SAR (ASAR) images are used to monitor the water-area variations of Dongting Lake, China. Results demonstrate the effectiveness of the time series of SAR imagery to monitor changes in water-basin extent. The same lake is analyzed in Xing et al. (2018) using dual-polarization (DP) C-band Sentinel-1 (S-1) SAR imagery. The authors adopt an empirical threshold to generate a binary image where the water body is distinguished from the surroundings. In addition, it is shown that the vertical transmit and horizontal receive (VH) channel outperforms the vertical transmit and vertical receive (VV) one in identifying surface water. In Li and Wang (2015), Otsu's method is used to detect water bodies in the Spiritwood buried valley using full-polarimetric (FP) C-band RadaRSAT-2 imagery. Experimental results show that the cross-polarized channel results in the best land/water discrimination. In Zeng et al. (2017), the water body of the Poyang Lake (China) is distinguished from the surroundings using a histogram-based threshold. Experimental results show that the dense time series of Sentinel-1 SAR imagery provides enough sensitivity to track monthly variations of the water body. In Masetti et al. (2018), the high-resolution (3 m) COSMO-SkyMed X-band SAR data are used to monitor the artificial recharge basin area of the Po plain, together with ground observations and numerical modeling. The study shows that the approach is reliable in estimating the total infiltration capacity. Finally, multi-polarimetric features are exploited in Ferrentino et al. (2020) to evaluate the changes in the reservoir water body of Monte Cotugno Lake (Italy). Results, obtained using a two-year time series of DP Sentinel-1 SAR data, show that DP metrics outperform single polarization (SP) ones in land/water separation.

Water content variations can also impact the land surrounding a water body producing ground subsidence/uplift which can be effectively monitored with millimeter accuracy by multi-temporal SAR Interferometry (InSAR) techniques (Stramondo et al., 2008; Wang et al., 2012; Polcari et al., 2018). Such effects typically occur on the river or lake banks and are mostly characterized by elastic or poroelastic deformation according to the ongoing phenomenon and the material response. The elastic deformation is characterized by ground subsidence or uplift as a consequence of the increasing or decreasing surface load mainly due to water mass increase in the ground and water bodies in rainy seasons and vice versa in dry seasons (Gahalaut et al., 2017; Vitagliano et al., 2020). On the other hand, poroelastic deformation is mostly connected with the changes in water head level in aquifers (Chaussard et al., 2014). When the water is withdrawn typically the deposits undergo compaction effects that result in ground subsidence, conversely, with the recharge, pores are refilled thus producing ground uplift (Bell et al., 2008; Béjar-Pizarro et al., 2017). The ground deformation occurring in areas surrounding water bodies has been studied by satellite InSAR data. The ground subsidence and uplift around Lake Mead, Nevada, induced by water level increase and drop according to the elastic behavior of the deposits is studied in Cavalié et al. (2007) using ERS 1-2 InSAR imagery. The Lake Mead area is also investigated in Darvishi et al. (2021) using ERS1/2, Envisat, ALOS, and Sentinel-1 data. The Siling Co Lake, in central Tibet, is studied in Doin et al. (2015) using ERS and Envisat SAR imagery, which measures subsidence of about 5 mm/yr associated with the increased lake load. The elastic response to water level changes around Yangzhuoyong Lake, Tibet, is investigated in Zhao et al. (2016) using Envisat SAR data. The subsidence around Lake Nasser, Egypt, is modeled in Saleh et al. (2018) and linked to the loading of the lake. The significant long-term subsidence affecting the Yellow River Delta, China due to groundwater exploitation is addressed in Yi et al. (2021) showing the key role of poroelastic effects.

In this study, the drought phenomenon that affected the Po River in 2022 is analyzed by jointly exploiting two different SAR-based techniques and meteo-climatological information. The proposed SAR processing has a twofold objective: to estimate the water-covered area and track it over time; and to augment the previous estimates with vertical ground deformation obtained through InSAR processing. These two approaches are applied to a 7-years time series of Sentinel-1 SAR scenes collected over a region of interest close to the city of Piacenza, Italy, which includes the Po River (Fig. 1). This region is selected since here the river calls for a complex shape, pushing the limits of the applied SAR techniques. The meteo-climatological information, which is here used to provide independent validation of the SAR-based estimated trends, includes hydrometric water level, rainfall data, and Standard Precipitation Evapotranspiration Index (SPEI). Experimental results show that the water area estimated by the proposed approach fits in-situ observations and is consistent with the InSAR-based measurements. In addition, the approach allows the detection of both seasonal and inter-annual trends, such as harsh drought phenomena.

The main innovative contributions of this study can be summarized as follows: (a) the extraction of the water-body area, which is a quite challenging task in the case of rivers due to their relatively small bank-to-bank extension, is here addressed using both co- and cross-polarized Sentinel-1 scenes showing that the former provides generally more accurate results; (b) the time variability of the water-body area is here investigated using a 7-year SAR time series that clearly emphasize the anomalies associated to drought events confirmed by external meteo-climatological information; c) the joint use of the proposed SAR (water-body extent) and InSAR (vertical displacement) products can help to monitor the effects of climate variation affecting the Po river basin, and in particular, the drought phenomenon impacting this area in the last years.

Although here we showcased the results on a portion of the Po River, the wide swath of the Sentinel-1 mission makes the proposed approach potentially applicable to regional scale studies, including the entire hydrologic basin, and the network of tributaries, and to other river basins, especially those located in remote areas, which are hard to monitor through in-situ measurements. In addition, the joint use of SAR-based and meteo-climatological information is shown to provide useful information for monitoring the climate variation effects at unprecedented spatial scales and spatiotemporal resolution.

2. Area of interest and datasets

2.1. Study area

The study area is depicted as a red box in Fig. 1 and includes the Po River area close to the city of Piacenza, in Northern Italy. The Po is the longest Italian river, stretching over 650 km from its source in the Western Alps to the Adriatic Sea. The river flows through several Italian regions, including Piemonte, Lombardia, Emilia-Romagna, and Veneto, and has a catchment area of approximately 71,000 km^2. The area surrounding the river is characterized by a mix of agricultural, industrial, and urban land uses. The area is also densely populated hosting more than 15 million people (Bodini et al., 2000). The Po River and its tributaries are essential resources for the region's water supply, irrigation, and hydropower production. However, the basin experienced several droughts in recent years, leading to significant water scarcity and economic losses (Damilano, 2022). The most recent drought was so impressive that its effect can be observed by visually inspecting the two optical images of Fig. 2 which were collected on November 18, 2018, i.e., before the drought event (a), and on July 18, 2022, i.e., during one of the peaks of the drought (b).

2.2. Data sources

The SAR dataset consists of a time series of 217 C-band S-1 images collected in Interferometric Wide (IW) mode over an area that includes the Po River, from June 27, 2015, to September 18, 2022. This dataset is used to estimate the water content and to perform the InSAR analysis. The S-1 images are acquired along the ascending pass with an incidence angle of around 39°. An excerpt of the speckle-filtered VV SAR scene acquired on November 14, 2018, i.e., before (Fig. 3(a)) and July 20,

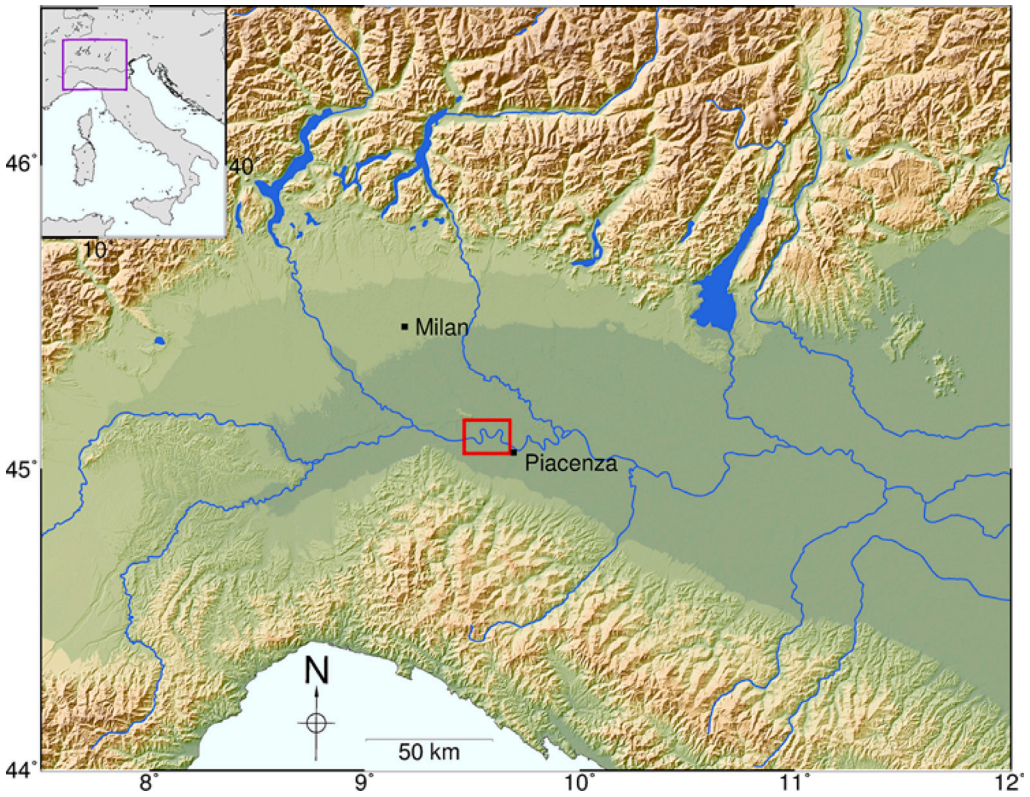

Fig. 1. Pictorial view of the area that hosts the Po River. The red rectangle shows the selected region of interest adopted in this study. (For interpretation of the references to color in this figure legend, the reader is referred to the web version of this article.)

2022, i.e., during one of (Fig. 3(c)) the major droughts occurred in 2022 is here presented for reference purposes.

The ancillary datasets include information on meteo climatic trends: hydrometric water level, rainfall data, and Standard Precipitation Evapotranspiration Index (SPEI). The hydrometric water level data are recorded at the Piacenza station (ID 210700) from the Agenzia Interregionale per il fiume Po (https://idrometri.agenziapo.it/Aegis/map/map2d). The rainfall data refer to the Piacenza area (cell number 0288) and are extracted from a climate dataset produced by the Arpae Climate Observatory (https://dati.arpae.it/dataset/erg5-eraclito) (Antolini et al., 2016). This dataset covers the whole Emilia Romagna region and is obtained by spatially interpolating on a regular grid the values measured by a network of meteorological stations.

The SPEI (Vicente-Serrano et al., 2010) is a multi-scalar drought index based on precipitation and potential evapotranspiration. It combines input data (e.g., rainfall and temperature) with climate and statistical analysis to compute anomalies (i.e., deviations from the long-term average) of the observed total surface water balance (difference between precipitation and potential evapotranspiration) for any location and time scale (1 month to few years). Therefore, the SPEI index can be used to determine the onset, duration, and severity of dry/wet conditions (respectively positive/negative SPEI values) in a variety of environments. The SPEI is usually calculated on a daily basis on different time scales and using a predefined time span (decades) as the reference period. The time scale (accumulation period) corresponds to the length of the rolling time window over which the total surface water balance is calculated: 30 days for SPEI-1, 60 days for SPEI-2, 90 days for SPEI-3, and so on. The SPEI output consists of positive and negative values, with SPEI≈0 representing normal conditions of surface water balance in the selected time scale compared to the long-term average, SPEI≈1/-1 representing a surplus/deficit of about one standard deviation in surface water balance (wet/dry conditions). SPEI values <–1 typically indicate moderate-to-severe drought periods.

Different SPEI datasets exist, which are obtained using different input data, model assumptions, and spatial resolutions. In this study, the SPEI data provided by the Alpine Drought Observatory (https://ado.eurac.edu/ Slovenian Environment Agency, & Central Institution for Meteorology and Geodynamics, 2022) are used, since they include a detailed analysis of the Alpine area performed using a time scale consistent with the time period analyzed. We selected data referring to the area of Lodi and Pavia provinces, which are adjacent to our study area, and we considered different accumulation periods.

3. Methodology

The methodology to process the SAR dataset includes the estimation of the water body area and deformations occurring along the banks of the Po River.

3.1. Water body area estimation

The water body area is estimated from the Sentinel-1 scenes using a constant false alarm rate (CFAR) approach that binarizes the Sentinel-1 scene to distinguish the water body from the surroundings. The methodology consists of the following steps.

The first step is to pre-process the SAR data set by performing: (a) radiometric calibration to convert image pixel values to normalized radar cross section (NRCS); (b) speckle noise reduction using an N×N boxcar filter. In this study $N = 7$ is used since it provides a good enough trade-off between speckle reduction and spatial resolution; (c) terrain correction to convert the SAR imagery from slant to ground range coordinates using the digital elevation model (DEM) obtained from the Shuttle Radar Topography Mission (SRTM) 1 Arc-Second, i.e., 30 m spatial resolution; (d) resampling to generate square-pixel images of 13.9 m by 13.9 m; (e) multi-temporal coregistration of all the scenes onto a common grid. Once the pre-processing is accomplished, the co-polarized NRCS is used to generate the binary map.

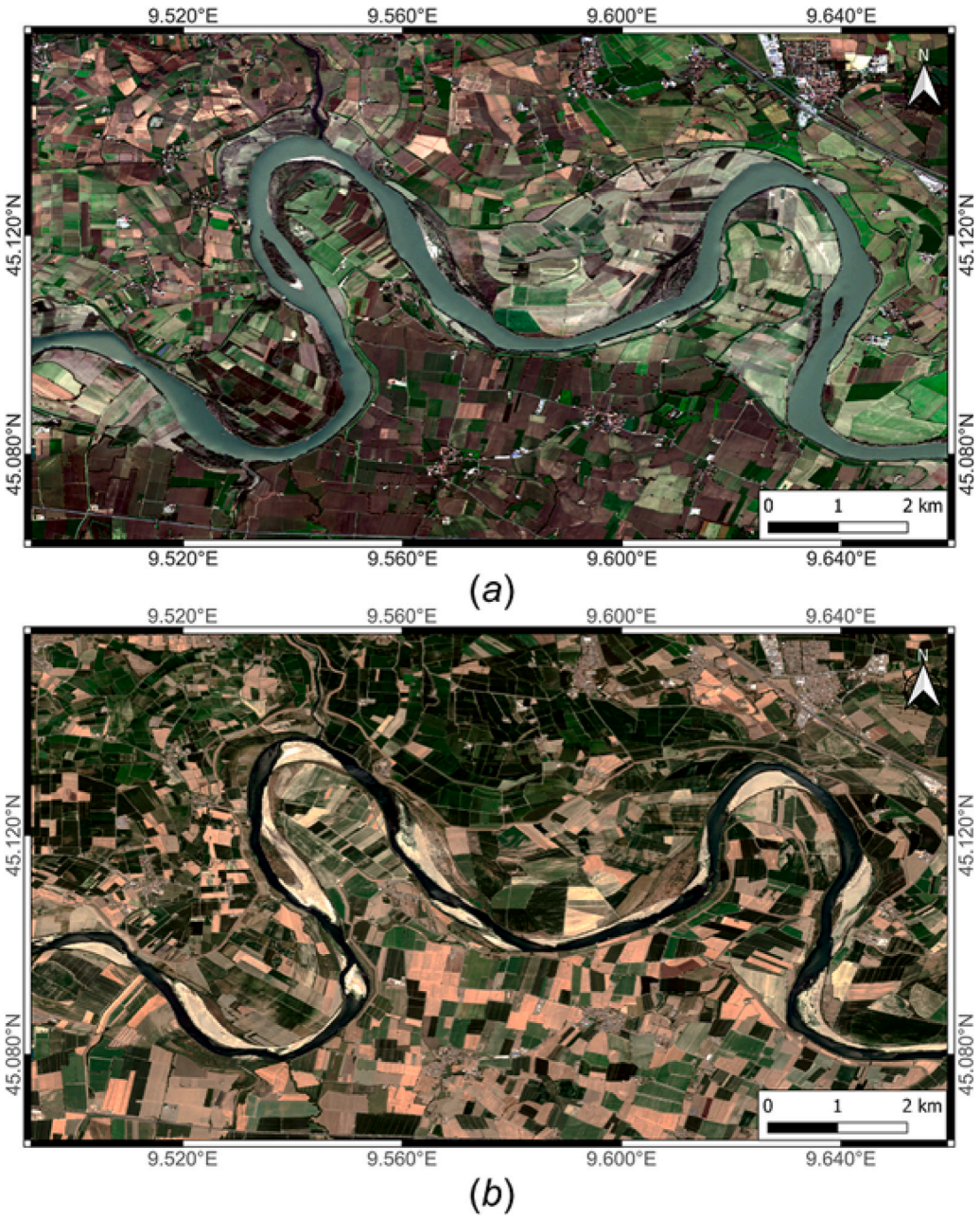

Fig. 2. Excerpt of the Sentinel-2 scenes acquired on November 18, 2018 (a) and July 18, 2022 (b) over the area of interest.

The second step is to generate a binary image by contrasting each pixel with a threshold. To cope with the speckled nature of the SAR imagery, a CFAR method is applied to the NRCS image. A key step to designing a CFAR method is studying the spatial distribution of the NRCS over the clutter, i.e., a region that belongs to the water body of the Po River. In Ferrentino et al. (2020), the NRCS distribution over the water-covered area is found to follow a Generalized Gamma Distribution (GΓD). According to the GΓD distribution, the CFAR threshold is given by:

$$\text{th} = \begin{cases} \sigma \left(\frac{1}{\mu} \Gamma^{-1} \left(1 - P_{\text{fa}}, \mu \right) \right)^{\frac{1}{\nu}}, & \nu > 0 \\ \sigma \left(\frac{1}{\mu} \Gamma^{-1} \left(P_{\text{fa}}, \mu \right) \right)^{\frac{1}{\nu}}, & \nu < 0 \end{cases} \tag{1}$$

where P_{fa} is the pre-assigned probability of false alarm, $\Gamma(\cdot)$ is the Gamma function, σ, and μ represent the non-negative scale and power parameters, respectively, and ν is the shape parameter (Stacy, 1962).

The final step consists of extracting the edges of the binary map that can be considered as the waterlines of the river. Once the latter is available, the water body area is straightforwardly obtained by counting the number of pixels within the waterlines and weighting them according to the Sentinel-1 pixel size.

3.2. Ground deformation estimation

The ground deformation estimates are obtained using the InSAR technique. It is well known that ground movement and topography changes that occurred between two SAR acquisitions can be estimated through the interferogram (Massonnet et al., 1993), that is the pixel-by-pixel phase difference between the two SAR images. When using large datasets of SAR images acquired for long-time spans, several interferograms can be calculated and combined to reconstruct the temporal deformation history of all the InSAR point targets identified in the area of interest. In the last two decades, several methods have

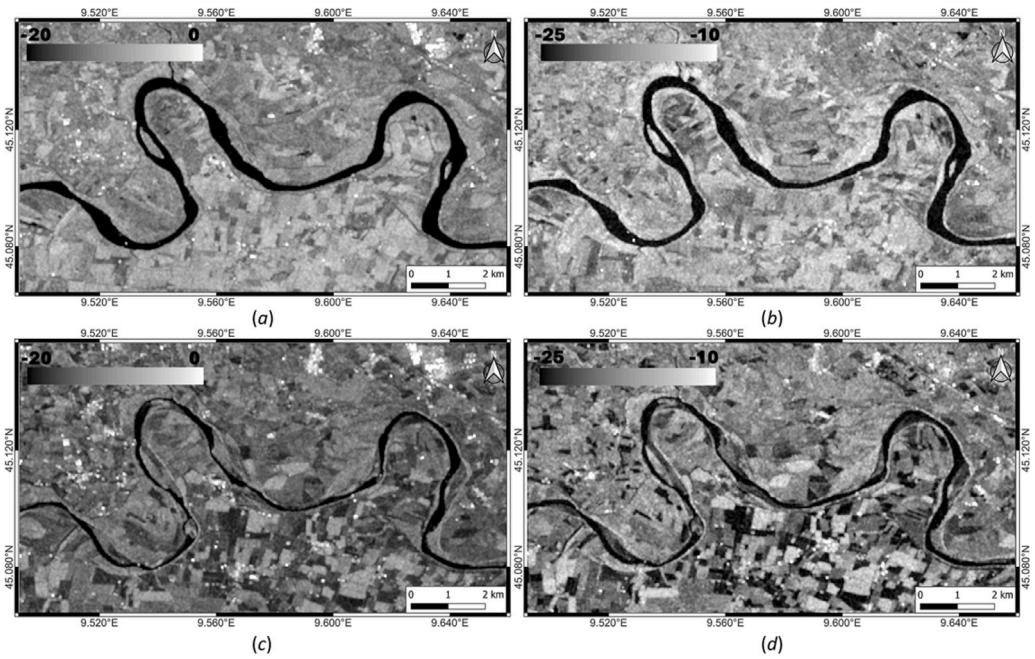

Fig. 3. Excerpt of the Sentinel-1 speckle-filtered SAR scenes collected on November 14, 2018 (a, b), i.e., before the main drought events, and on July 20, 2022 (c, d), i.e., during one of the main drought events. The first column (a–c) and the second column (b–d) stand for VV- and VH-polarized SAR scenes.

been developed (Crosetto et al., 2016) to reconstruct such information, all relying on the two main techniques proposed more than two decades ago: the Permanent Scatterers (PS, Ferretti et al., 2001), and the Small Baseline Subset (SBAS, Berardino et al., 2002). Here, the S1 dataset acquired from 2015 to 2022 is processed by a multi-temporal InSAR approach developed and implemented in the GAMMA software (Wegmuller, 1997). The data are first multi-looked by factors of 24 by 6 to reduce phase noise thus obtaining a pixel spacing of about 90 m. Then the interferometric pairs are selected by setting a maximum threshold for the spatial and temporal baseline to 100 m and 100 days, respectively, returning in 1355 interferograms. A 30 m spatial resolution DEM, provided by the SRTM mission, is then used to remove the topography-related phase and the retrieved interferograms are filtered by Goldstein filter (Goldstein and Werner, 1998), unwrapped by Minimum Cost Flow algorithm (Costantini, 1998). The interferograms affected by severe tropospheric artifacts and unwrapping errors are manually removed. The whole stack of interferograms is spatially sampled to extract point targets following coherence threshold criteria, i.e., identifying all the points in the interferograms that can be assumed as persistent in all the SAR images in the stack. Finally, ground deformation velocity and displacement time series are estimated using an extension of the Singular Value Decomposition (SVD) based on Least-Squares inversion (Werner et al., 2012; Berardino et al., 2002).

4. Results and discussion

This section discusses the experimental results related to the estimation of the water body area and the ground deformation and their comparison with ancillary data.

4.1. Water body area estimation

In this subsection, first, the sensitivity of the waterline extraction method is analyzed using selected test cases; then, the time-variability of the water body area is analyzed using a time series of 88 S-1 images (one per month from June 2015 to September 2022).

The sensitivity analysis consists of discussing the ability of the waterline extracted by the co- and cross-polarized NRCSs to fit the edges of the Po River. This task is carried out considering two meaningful SAR scenes, displayed in Fig. 3 according to a matrix format where the two rows consist of the imagery acquired before and during the major drought event that occurred in 2022; while the two columns stand for the VV- and the VH-polarized NRCSs. In all the images, the river appears darker than the background as expected since, from an electromagnetic viewpoint, the water body represents a smooth surface resulting in a backscatter lower than the surroundings, which in turn appears, in the SAR scene, darker than the background. By visually comparing the scenes collected before (first row in Fig. 3) and during (second row in Fig. 3) the drought event, we can note that the darker area associated with the water body reduces its size during the drought in both the polarimetric channels (see panels (c) and (d) in Fig. 3). This means that both co- and cross-polarized NRCSs provide information about the loss of water-covered areas resulting from the drought. In addition, there is also a fairly good visual agreement between the SAR imagery of Fig. 3 and the Sentinel-2 scenes displayed in Fig. 2. By visually inspecting the two polarimetric channels one can note that the area covered by the water does not change significantly in the pre-drought event (see panels (a) and (b) in Fig. 3); while non-negligible differences appear in the co- (c) and cross-polarized (d) imagery collected during the drought event.

To quantitatively analyze the area of the water-body estimated using σ^0_{VV} and σ^0_{VH}, the waterline is extracted according to the proposed methodology using a $P_{fa} = 10^{-6}$, that resulted in the best compromise in terms of water body detection/false alarms. The obtained binary image is then refined with a morphological filter, which consists of removing artifacts and filling holes. Finally, the waterline profile is extracted from the binary image using the Sobel edge detector algorithm (Raman and Aggarwal, 2009). A small portion of the region of interest (ROI) excerpted over the true-color Sentinel-2 scene collected before the event, is displayed in Fig. 4(a); while the corresponding σ^0_{VV} and σ^0_{VH} imagery are displayed in Fig. 4(b) and (c), respectively where the extracted waterlines are annotated as red lines. The extracted waterlines follow remarkably well the river profile and no false edge is visible. Negligible differences appear in the two extracted waterlines that can be likely due to the SAR processing. The robustness and accuracy of the waterline extraction process depend, of course, on the land/water separability. Therefore, to investigate

land/water separability in a more quantitative way, co- and cross-polarized NRCSs are evaluated along with the white dashed transect of Fig. 4(b) and, depicted in Fig. 4(d), where a decibel (dB) scale is used. The co- and cross-polarized NRCSs are represented using circle red and square blue markers, respectively. Note that the plot also shows the S-1 noise equivalent sigma zero (NESZ) value (−22 dB) that is annotated as dashed black line, together with the thresholds th_{VV} and th_{VH} automatically selected by the CFAR approach to process the σ^0_{VV} and σ^0_{VH} imagery, respectively (see dashed red and blue lines). In Table 1, the th_{VV} and the th_{VH} values are listed together with the sample at which the values are reached. By jointly analyzing Fig. 4(d) and Table 1 one can note that the two channels estimate a river bed extent equal to 570 m (co-pol) and 598 m (cross-pol). To verify the estimation accuracy, unfortunately, no ground information is available; hence, we used optical measurements to carry out an independent comparison. The Sentinel-2 optical image is processed through the Normalized Difference Water Index (NDWI) which emphasizes values associated with the water-covered area (McFeeters, 1996). The NDWI values evaluated along with the transect depicted in Fig. 4(b) are displayed in Fig. 4(d) as a pink line with square markers. Note that the NDWI threshold th_{NDWI}, that is empirically set to 0.4, is also annotated as a pink dashed line. The th_{NDWI} and the samples at which this metric is reached in both the upper and the lower banks of the Po River are listed in Table 1. The extent of the river bed estimated by the NDWI is equal to 626 m. Assuming the NDWI as a reference, both the SAR channels provide results comparable to the NDWI one (the difference is within 10 pixels) with the cross-polarized channel providing the best agreement. In addition, the main difference among the three metrics applies to the lower bank. From an electromagnetic viewpoint, it is worth noting that the cross-polarized signal is entirely below (above) the NESZ over the water body (surrounding land). The co-polarized NRCS is everywhere above the NESZ. To verify the ability of the co- and cross-polarized channels to extract the waterline during the drought event, the SAR scenes of Fig. 3(b) and (d) are processed. The ROI extracted on the true-color Sentinel-2 scene is depicted in Fig. 5(a) and the correspondent σ^0_{VV} and σ^0_{VH} imagery are displayed in Fig. 5(b) and (c), respectively where the extracted waterlines are also annotated as red lines. The scenario is completely different from the previous one since the drought event makes the river body very narrow in some areas where sand appears (see the blue and the red dashed boxes in Fig. 5(a) that show sandy areas that are not present in the image of Fig. 4(a)). By visually contrasting the σ^0_{VV} and σ^0_{VH} imagery of Fig. 5(b) and (c), significant differences appear with the σ^0_{VH} image resulting in a large number of false edges over the land area. In addition, the areas enclosed in the boxes annotated in Fig. 5(a) appear not correctly identified by the σ^0_{VH} processing. This can be observed also in the transects depicted in Fig. 5(d) where the same format of Fig. 4(d) is adopted. The waterline extracted using the σ^0_{VV} channel results in a fairly good agreement with the NDWI one, see Table 1; while the cross-polarized channel is not able to distinguish the water body neither from the sandy area (in the southern part of the bank) nor from the agricultural area (in the northern part of the bank). According to Table 1 and Fig. 5(d), when dealing with the upper bank, the pixels where the threshold values are reached in the co- and cross-polarized channels are close to the NDWI one. Significant differences apply when dealing with the lower bank. In this case, the σ^0_{VH} does not provide accurate enough results since it does not distinguish the water body from the sandy area. This is likely due to the low backscatter resulting from the water body and the sandy area, which is largely below the NESZ. All this matter demonstrates that the scattering peculiarities that characterize the river under the drought event suggest using σ^0_{VV} for the subsequent analyses since it provides the most accurate extraction of the water-body area.

The binary images obtained from σ^0_{VV} related to the Sentinel-1 imagery of Figs. 3(a) and (c) are shown in Fig. 6(a) and (b), respectively. The figure highlights the significant loss of water-covered area that occurred in the Po River from November 2018 to July 2022.

Table 1
Values of the CFAR thresholds corresponding to the selected P_{fa} for both the VV and the VH channels and pixel number at which the threshold is reached both in the upper and in the lower bank of the Po River. NDWI threshold and pixel at which the threshold value is reached on both the upper and the lower bank. The distance column refers to the distance (m) between the pixels lying in the upper and low banks.

Date	Threshold		Sample		Distance [m]
			Upper bank	Lower bank	
November 2018	th_{VV}	−17.2	37	78	570
	th_{VH}	−21	34	77	598
	th_{NDWI}	0.4	36	81	626
July 2022	th_{VV}	−17.8	37	48	153
	th_{VH}	−21	36	77	570
	th_{NDWI}	0.4	36	55	264

The number of pixels belonging to the water body (coded in black in the binary imagery) reduced significantly in Fig. 6(b). It can be also observed that, in some areas, the river is too narrow to prevent correct CFAR processing. Once the binary image that distinguishes the water body from the surroundings is obtained, the water body area can be straightforwardly evaluated by using the Sentinel-1 pixel size (which is equal to 13.9 m^2).

The value in square km of the water body area estimated within the area of interest of Fig. 1 over the whole time series of Sentinel-1 SAR scenes (one per month) is depicted in Fig. 7. The plot shows an oscillating trend that never decreases below 7 km^2, except for the period starting around summer 2022 that calls for a significant decreasing trend that reaches a maximum water loss in 2022. This result agrees with the independent information provided by the Po River district basin authority which reported a sharp reduction of the water area in the 2022 summer time (Clifford, 2022).

4.2. Ground deformation from InSAR

The ground deformation occurring along the banks of Po River is estimated using a data set of 215 S-1 images collected from June 2015 up to September 2022. The Line of Sight (LOS) ground deformation velocity estimated by InSAR analysis is shown in Fig. 8. Note that, due to the S-1 incident angle of around 39°, the LOS component accounts for about 75% of the total vertical displacement, assuming a negligible or null horizontal motion. A linear subsidence peaking at about 10–15 mm/yr is detected along the Po River banks. This trend is consistent with a typical river plain where the soft alluvial sediments may result in consolidation processes or anthropogenic activities such as water pumping or construction of infrastructures that result in ground subsidence phenomena (Stramondo et al., 2008; Polcari et al., 2014). This is what typically happens in the Po plain which is notoriously characterized by long-term subsidence, especially in the delta region (Baldi et al., 2009; Serpelloni et al., 2013). To mitigate the noise of InSAR data that may result in several outliers, the displacements estimated at the point targets located along the Po River banks (see the red polygon depicted in Fig. 8) are averaged at each epoch (Fig. 9(a)). Moreover, to remove the long-term effect and highlight seasonal and inter-annual variations, the average time series are detrended (Fig. 9(b)).

Fig. 10 shows the comparison between the water body (blue lines) and the InSAR time series (red lines). To make the two data sets consistent, the InSAR time series is first monthly averaged and then projected along the vertical displacement component (Fig. 10(a)). To better emphasize transient trend with respect to the high-frequency noise, an additional 6-month moving average window is applied (Fig. 10(b)); while the cumulative detrended time series are displayed in Fig. 10(c). The comparison between the two datasets shows that the two-time series are roughly in counter-phase: the increase in the water body area results in a decrease of the vertical displacement (subsidence) and, vice versa, the river banks uplift when the water body area decreases. This behavior applies, in particular, starting from mid-2021 till the

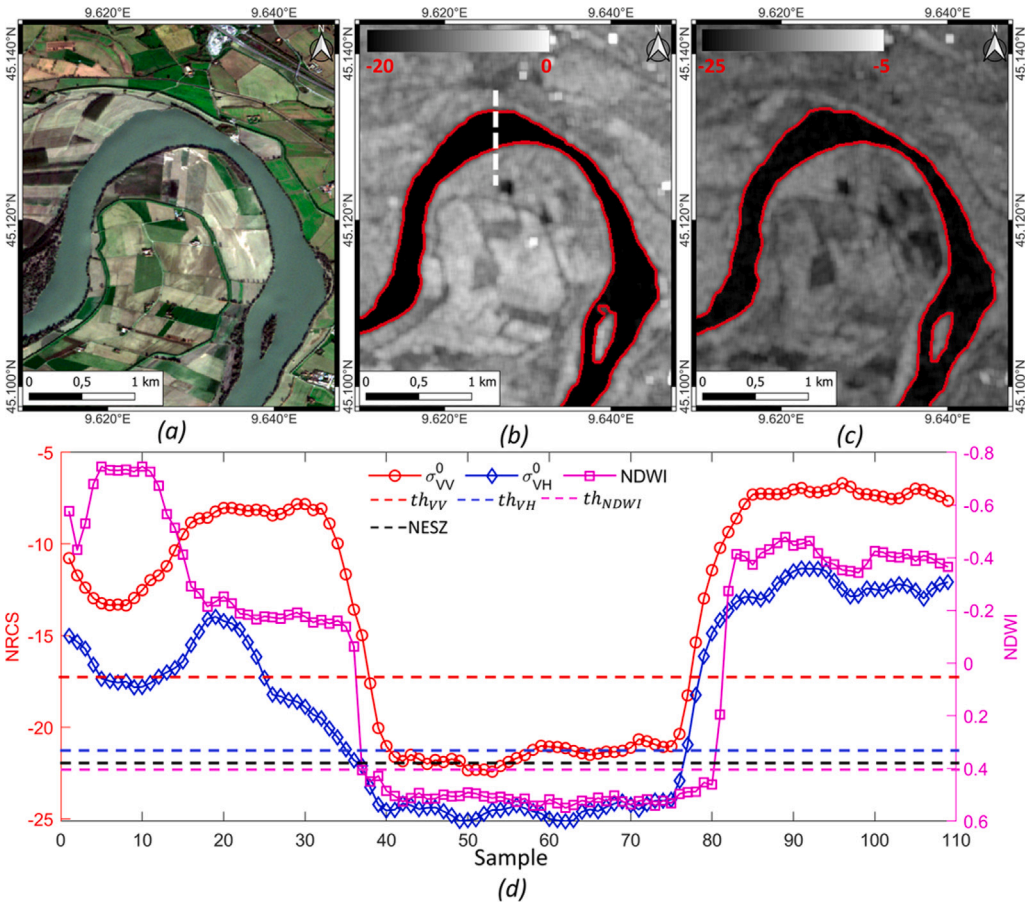

Fig. 4. (a) Excerpt of the Sentinel-2 image that includes the Po River observed on November 18, 2018; (b) and (c) waterline extracted from σ^0_{VV} and σ^0_{VH} input images and superimposed on the original VV- and VH-polarized NRCS SAR imagery, respectively, on November 14, 2018; (d) σ^0_{VV} (circle red curve), σ^0_{VH} (diamond blue curve) and NDWI (squared pink curve) evaluated along with the transect shown in panel (b).

end of 2022, i.e., during the 2022 drought where a cumulated uplift of about 6 mm is observed. This suggests that, at seasonal and inter-annual time scales, the alluvial deposits over the banks of the Po River mainly show an elastic response to water load: they subside when loaded by an external source such as an increase in river water level, surface water accumulation, and vice versa in the drought periods. This behavior is consistent with literature studies carried out at different spatial and temporal scales, with InSAR and other deformation data (Global Navigation Satellite System – GNSS) (Li et al., 2020; White et al., 2022). Even if at different spatial scales (basin area of Po River compared to the local area along the riverbanks we are addressing in this study) and spatial resolution (tens of kilometers for GNSS sites and hundreds of meters for InSAR points), a recent study based on vertical GNSS data shows that the whole Po River basin calls for an elastic response to hydrological loading, showing clear uplifting trend in drought periods (Pintori and Serpelloni, 2024). Future studies considering InSAR data over a larger area, and possibly incorporating GNSS data, could reveal information about the response of Po River basins to changing climatic conditions at unprecedented detail and provide key knowledge for water resource management. The additional complexity resulting from the InSAR time series is probably due to the superimposition of different types of responses expected by sedimentary material in river plains (Vitagliano et al., 2020). Furthermore, at least part of the observed InSAR signal could be related to the effect of soil moisture variations along the riverbanks. Indeed, as shown in literature, under specific conditions, the phase delay and the soil moisture exhibit a non-negligible correlation (De Zan et al., 2014; Ansari et al., 2021; Mira et al., 2022, 2024). This is due to the change of the dielectric constant between SAR acquisitions due to soil moisture variations which cause a deeper/shallower penetration of the SAR signal thus producing an apparent ground subsidence/uplift. Discriminating and quantifying the contributions of real and apparent deformation due to the elastic response and the soil moisture variations can be challenging. In any case, since both processes are related to changes in the water content in the ground, the correlation between InSAR displacement and the water body area remains valid.

4.3. Comparison with external data

To assess the reliability of the water body area estimates, the latter (blue curve in Fig. 11(a)) are contrasted with all the available ancillary data. To be consistent with the monthly temporal sampling of the SAR dataset, all ancillary data are sampled as mean monthly values. Firstly, the water-body area is contrasted with the hydrometric water level (red curve in Fig. 11(a)), which can be considered as external benchmark information that is used operationally by the District Basin Authority. It can be noted that the period under investigation shows seasonal and inter-annual variability of climatic conditions, where wet periods (e.g., 2018–2019, 2020–2021) alternate with dry ones (e.g.,2017–2018, 2021–2022). In the period spanning from mid-2021 to the end of 2022, the effect of the severe drought (Bonaldo et al., 2022) is observed, resulting in a hydrometric water level showing a quasi-monotonic decreasing trend that approaches −1.5 m. The curves of Fig. 11(a), exhibit a fairly good agreement demonstrating the ability of SAR to detect the seasonal trend and to highlight anomalies, such as the severe water loss associated with the 2017 and 2022 drought episodes. To highlight the transient deviations from the average long-term (2015–2022) behavior of water level and water-body area, the

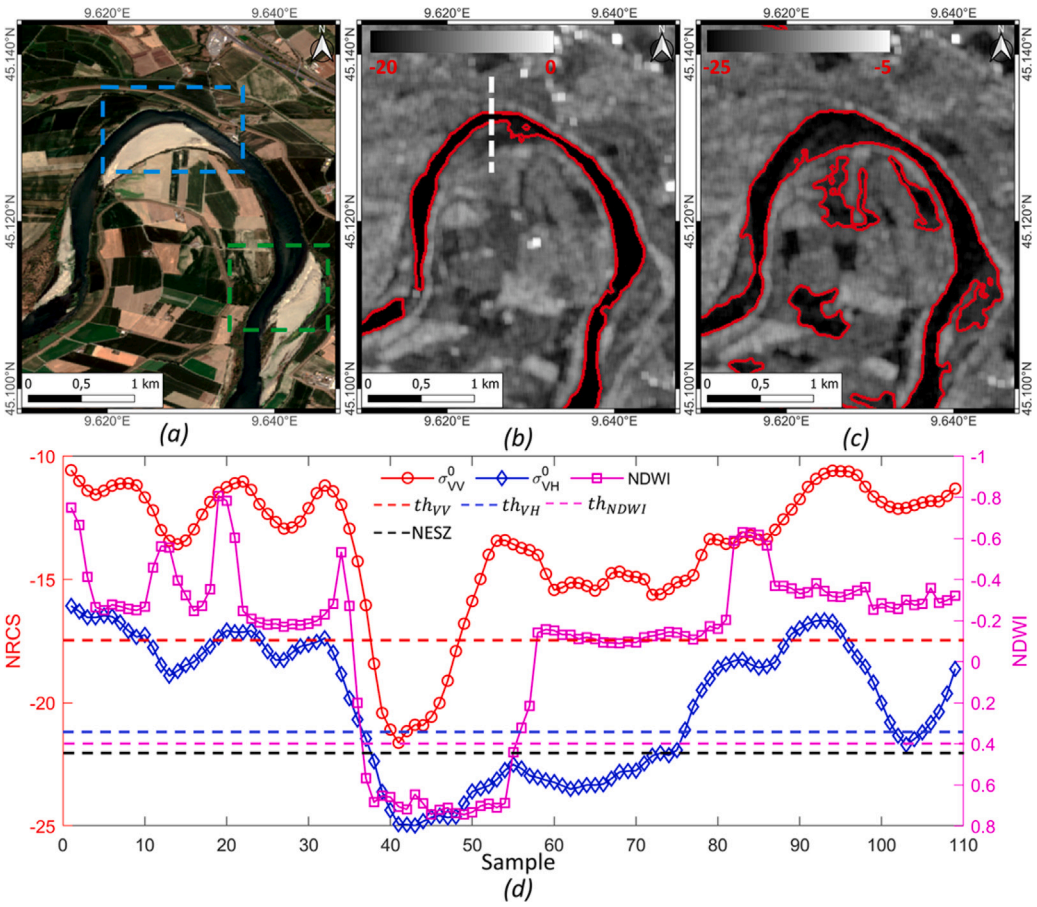

Fig. 5. (a) Excerpt of the Sentinel-2 image that includes the Po River observed on July 18, 2022; (b) and (c) waterline extracted from σ^0_{VV} and σ^0_{VH} input images and superimposed on the original VV- and VH-polarized NRCS SAR imagery, respectively, on July 20, 2022; (d) σ^0_{VV} (circle red curve), σ^0_{VH} (diamond blue curve) and NDWI (squared pink curve) evaluated along with the transect shown in panel (b).

cumulative-detrended time series is computed (i.e., first, the cumulative series is computed, and, then, a linear trend is fitted to the cumulative series and subsequently removed (Roeloffs, 2001)). The resulting time series (Fig. 11 (b)) presents a fairly good agreement, highlighting clearly alternated phases of dry and wet periods, as the steep decreasing trends associated with the 2017 and 2022 drought periods (Baronetti et al., 2020; Bonaldo et al., 2022). Moreover, we computed the cross-correlation between the SAR water body and the water level data, resulting in values higher than 0.7, at zero time lag, see Table 2. In Fig. 11(c) the water body area is contrasted with the monthly rainfall which represents one of the key factors affecting wet/dry periods. The figure shows a fair agreement between periods of low (high) rainfall rates and lower (higher) water-body areas. This is even clearer in Fig. 11(d) where the cumulative detrended time series are contrasted. It is worth noting that the decreasing trend observed in the rainfall data spanning from 2016 to 2017 is captured by the SAR estimates starting from late 2017. A time lag between the two curves applies while they are almost time synchronous in detecting the decreasing trend that occurred in 2022. This behavior can be also observed in Fig. 11(a) and (b) suggesting some intrinsic differences between the onset of the two drought episodes. The cross-correlation analysis confirms this result with a moderate correlation (0.65) with a three-month time lag between the two measurements. The monthly time series results in a lower correlation likely due to the scattered nature of monthly rainfall data. This indicates that the water body area mostly depends on trends of rainfall cumulated over time, instead of short-period rainfall variations.

The last comparison is with the SPEI indexes. The SPEI index is a comprehensive metric of the regional-scale behavior of the Po River, which, embeds multiple meteorological information (Section 2.2). The SAR water body area is compared with the SPEI related to different aggregation periods (1 month – SPEI-1 – to 12 months – SPEI-12) for the Pavia and Lodi areas. The cross-correlation analysis shows moderate values, slightly higher for the Pavia area with a maximum value (equal to 0.62) corresponding to SPEI-6 (Table 2). The comparison between the SPEI-6 time series and the water body area is shown in Fig. 12 which shows a good agreement between the short-term peaks in the water-body area and positive SPEI values. This could indicate that the water body area reflects both short (monthly) and medium-scale (years) climate time scales, possibly related to different drought types, i.e. droughts affecting only the shallower soil levels or deeper ones, affecting groundwater content (Vicente-Serrano et al., 2010). The same agreement also applies when dealing with a strong reduction of the water body area that corresponds to negative SPEI values. Note also that SPEI values lower than −1 (which indicate severe drought) correlate well with the reduction of the SAR-estimated water-covered area that occurred in 2021–2022. In general, discrepancies between the two datasets might be partly due to the different spatial scales involved.

To better understand the ground deformation affecting the river-bank, the estimated InSAR time series are contrasted with the rainfall and water level data, assumed as a proxy of the temporal trend of the main factors potentially causing surface loading/unloading (water accumulation/depletion in soil and river water level variation). Fig. 13 shows the comparison between monthly data (panels (a) and (c)) and after applying a 6-month moving average (panels (b) and (d)), which highlights inter-annual trends. All plots show that, at first order, dry periods are associated with uplift, and vice versa, in agreement with the elastic response to the elastic loading hypothesis presented in

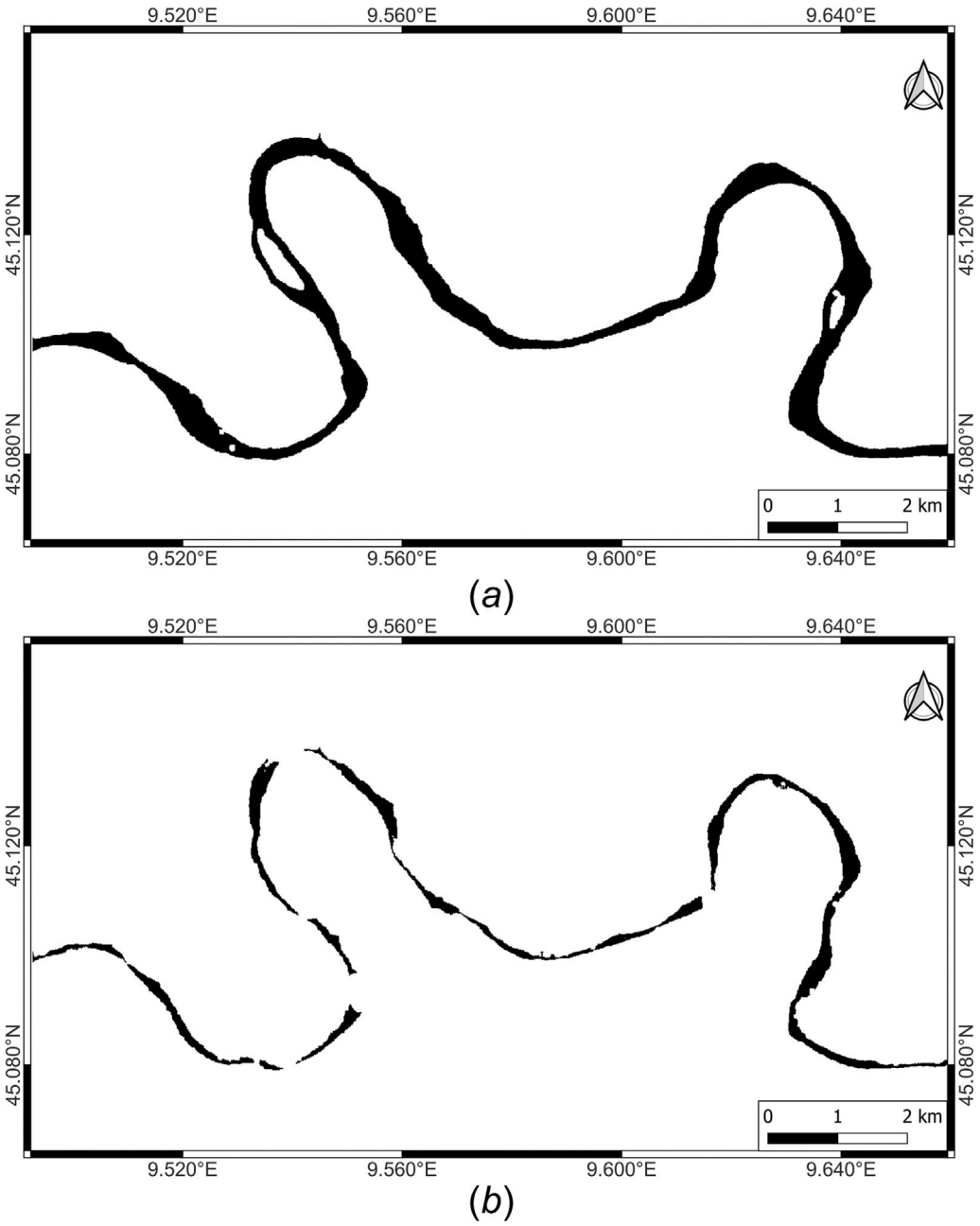

Fig. 6. Binary images related to the VV-polarized SAR scenes of Fig. 3 acquired before (a) and during (b) one of the major drought events.

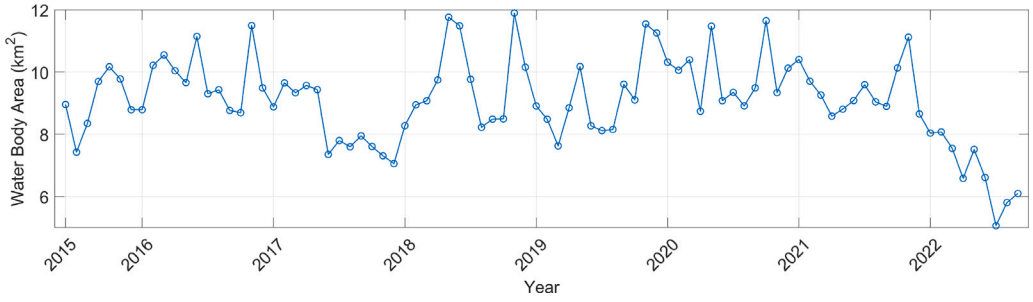

Fig. 7. Water-body area estimated from the binary images obtained by the time series of σ^0_{VV} imagery.

Section 4.2. Discrepancies and time-lags between the compared time series could be attributed to data uncertainties and different spatial resolutions, to further complexities affecting the InSAR data, as discussed in Section 4.2, and to the complex response of the soil to periods with climatic conditions of different intensity and temporal duration. These results suggest the use of InSAR ground deformation measurements to

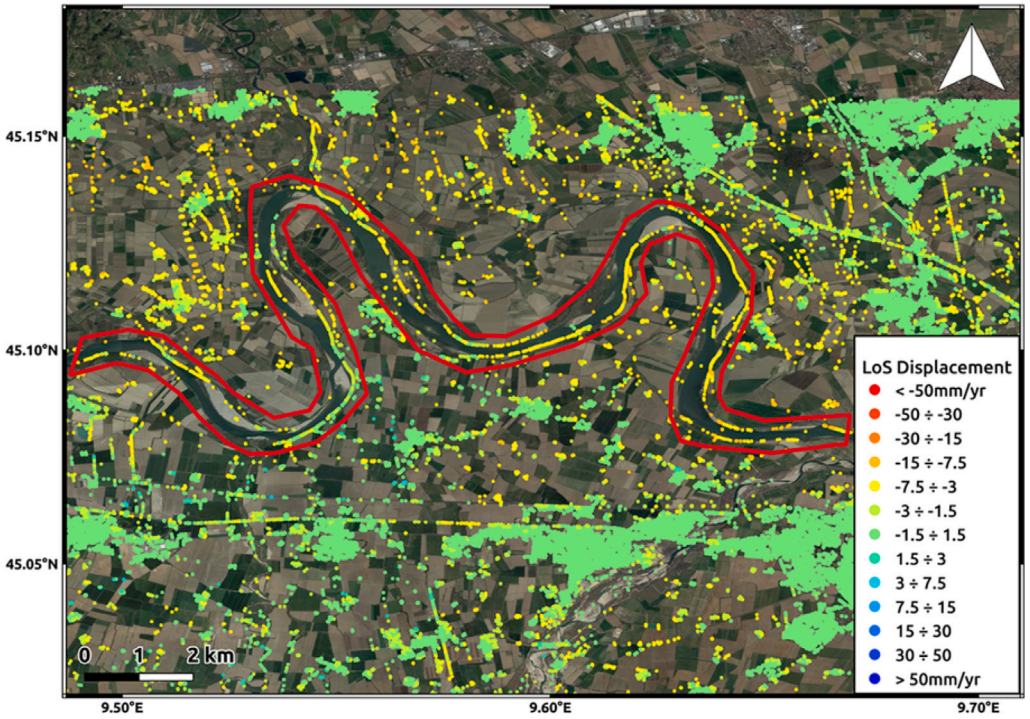

Fig. 8. LOS displacement estimated using the whole InSAR data set within the area of interest depicted in Fig. 2. The point targets are colored according to the displacement in mm/year. The polygon that will be used in the subsequent experiments is also annotated in red. (For interpretation of the references to color in this figure legend, the reader is referred to the web version of this article.)

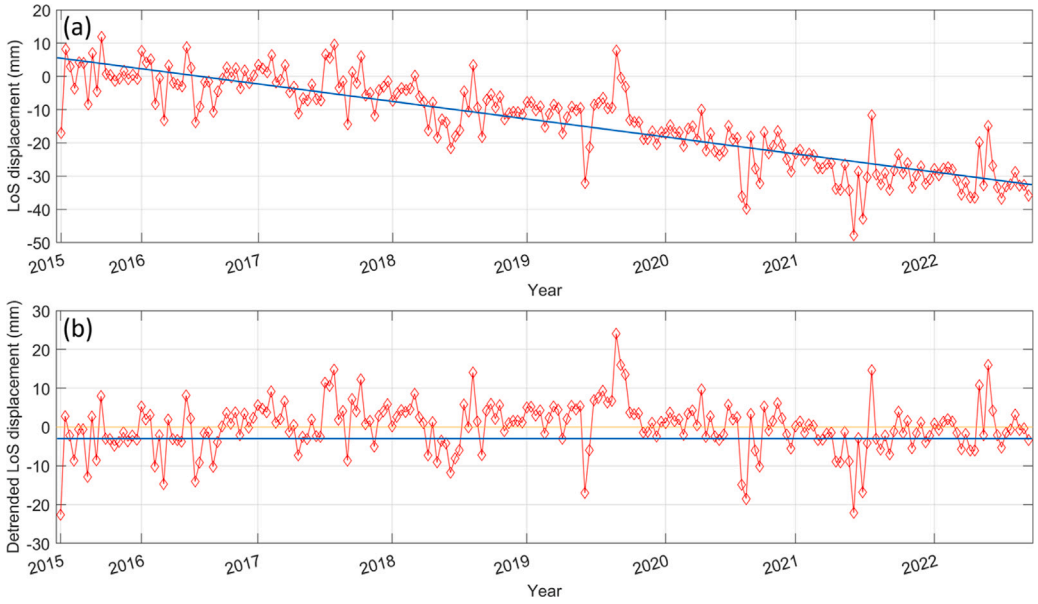

Fig. 9. The mean displacement (a) related to the point targets within the red polygon of Fig. 8 and its detrended (b) version. The blue line indicates the linear deformation trend.

cross-validate and support the interpretation of the water-body area results.

5. Conclusions

This study is to discuss the ability of multi-polarization Sentinel-1 SAR imagery to monitor variable conditions of river basins associated with different meteo-climatic trends, with a special focus on hydrological droughts, as the one that hit the Po River basin in 2022. Added-value products are derived from a 7-year time series of SAR and InSAR measurements to analyze the drought events through the water-area coverage and the ground displacements. These added-value products are then contrasted with meteo-climatological products to demonstrate their performance. Although the SAR-based processing is based on state-of-the-art approaches, the following novelties are introduced:

(a) The SAR method to extract the water-body area is applied to a challenging position of the Po River that calls for a very complex shape. Experimental results show that, unlike the literature that suggests using the cross-polarized channel to detect the waterline of inland basins, here the co-polarized channel performs best under drought conditions. We also elucidated the

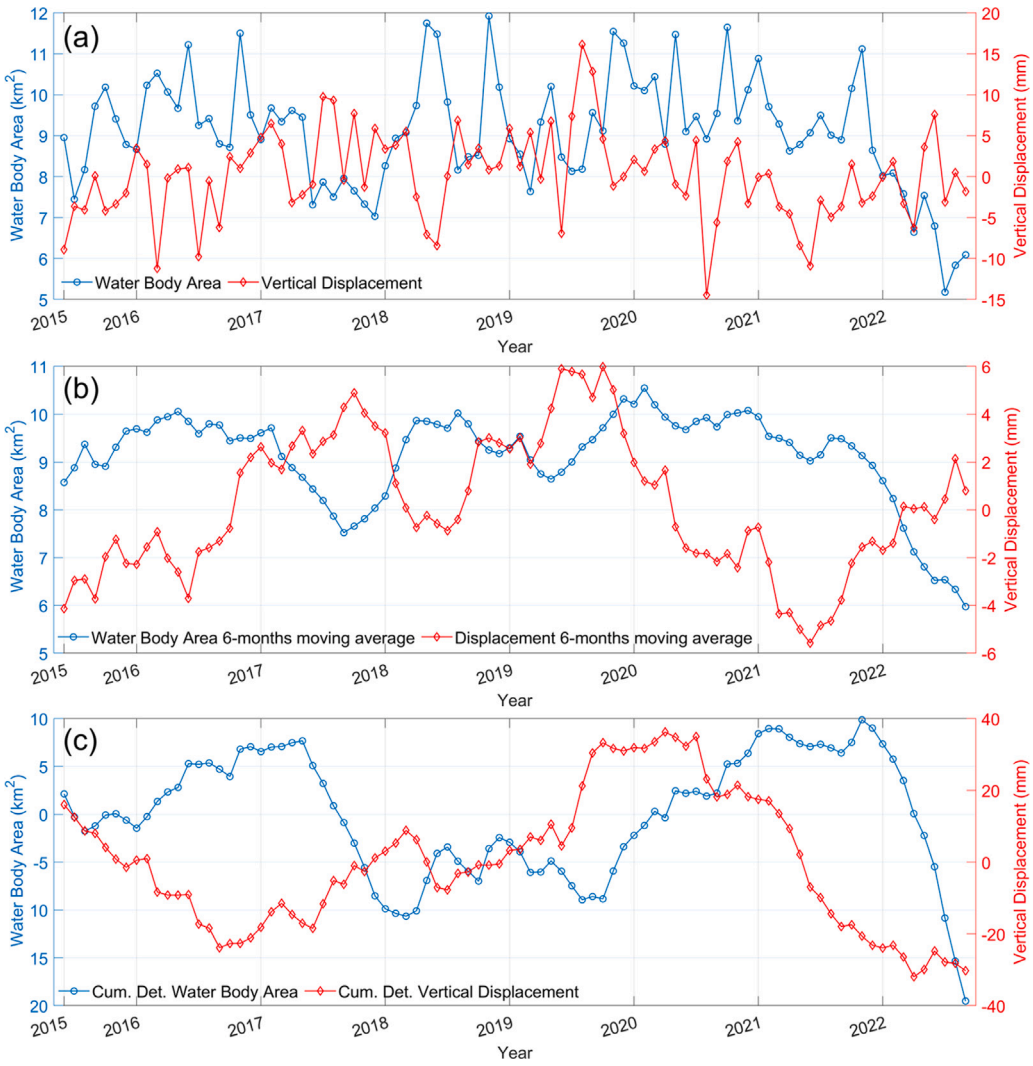

Fig. 10. SAR-based estimates are contrasted with external info. (a) Water body area against InSAR vertical displacement; (b) 6-month moving average water body area against 6-month moving average vertical displacement; (c) cumulated and detrended water body area against cumulated and detrended vertical displacement.

Table 2
Cross-correlation results between the water body area time series (and the related cumulative detrended time series) and the ancillary data time series.

Water Body Area VS	Correlation value	Time lag (months)
Rainfall	0.37	0
Cum. det. Rainfall	0.65	3
Hydrometric Water Level	0.80	0
Cum. det. Hydrometric Water Level	0.72	0
SPEI-1 (Pavia/Lodi)	0.45/0.35	0/0
SPEI-3 (Pavia/Lodi)	0.55/0.47	0/0
SPEI-6 (Pavia/Lodi)	0.62/0.54	0/0
SPEI-12 (Pavia/Lodi)	0.56/0.55	0/0

physical processes that are at the basis of this result, namely the occurrence of sandy areas (under drought event) that call for a backscatter indistinguishable from the water one using the cross-polarized channel.

(b) To the best of our knowledge, the SAR water-body area has never been contrasted with the InSAR-based ground displacement. Although there is still room for a deeper understanding of the physical processes linking the two information, this study paves the way to synergistic exploitation of ground motion and under-extent information.

An additional key novelty arising from this study consists of contrasting information derived by SAR (and therefore available on a fine spatial resolution scale over a dense enough time scale) with meteo-climatological information available at a different time and spatial scale/ Experimental results are convincing and can be summarized as follows:

(a) the time evolution of the water body area extracted from the time series of co-polarized Sentinel-1 imagery agrees fairly well with the independent hydrometric rainfall and SPEI information, suggesting including SAR-based analysis to help decision-makers;

(b) the ground deformation appears to be mainly linked to the elastic response of the riverbanks to the water load variation (subsidence in periods of increasing water level during the rainfall season and uplift in drought periods, as the recent one in 2021–2022). However, the effects of additional factors (e.g., inelastic deformation or processing inaccuracies due to soil moisture variation) cannot be excluded;

(c) the time evolution of the ground deformation clearly points out an anomalous behavior in 2021–2022 confirming the severity of the drought event.

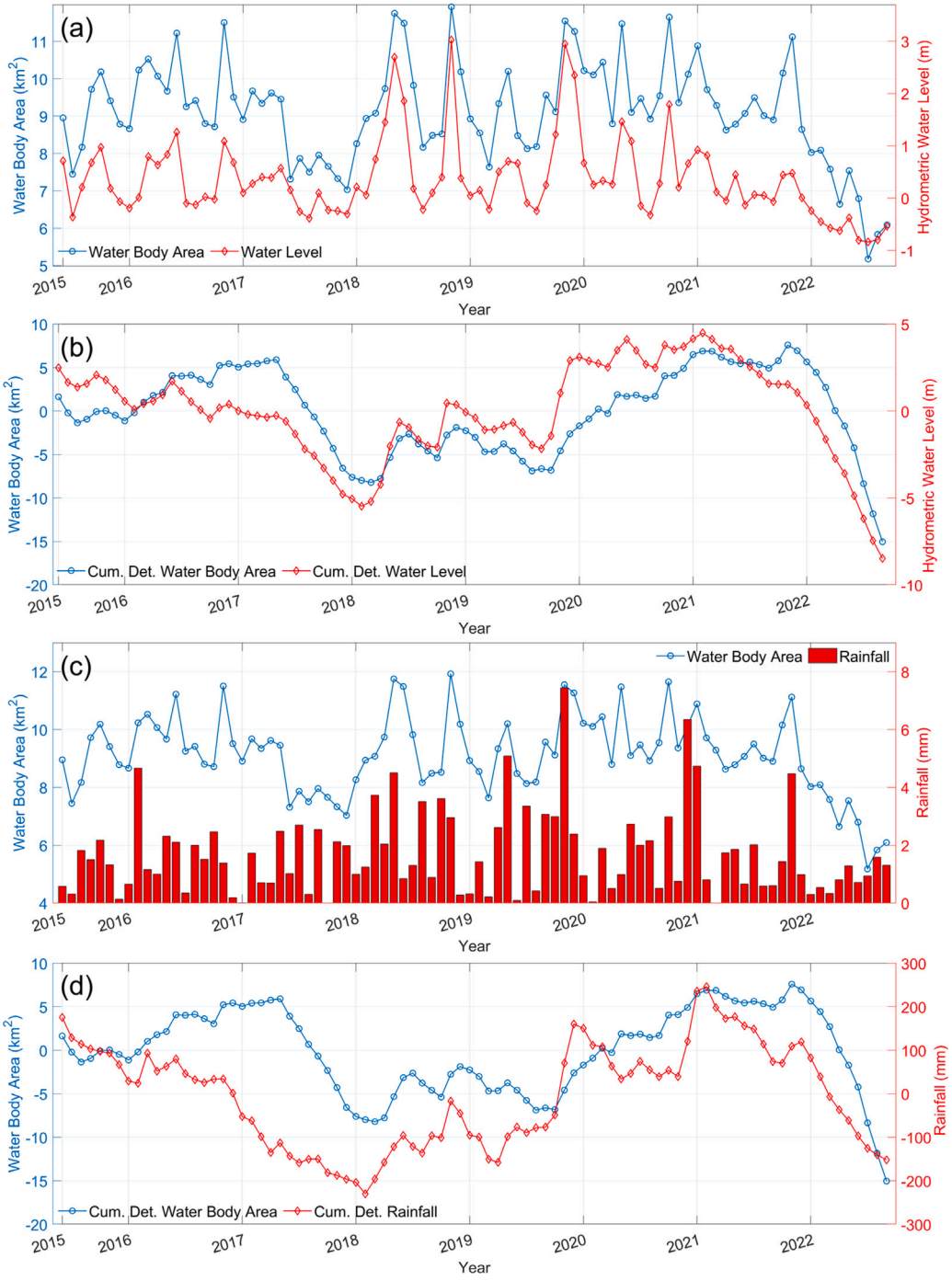

Fig. 11. SAR-based estimates are contrasted with external information. (a) Water body area against water level; (b) cumulated and detrended water body area against cumulated and detrended water level; (c) water body area against rainfall; (d) cumulated and detrended water body area against cumulated and detrended rainfall.

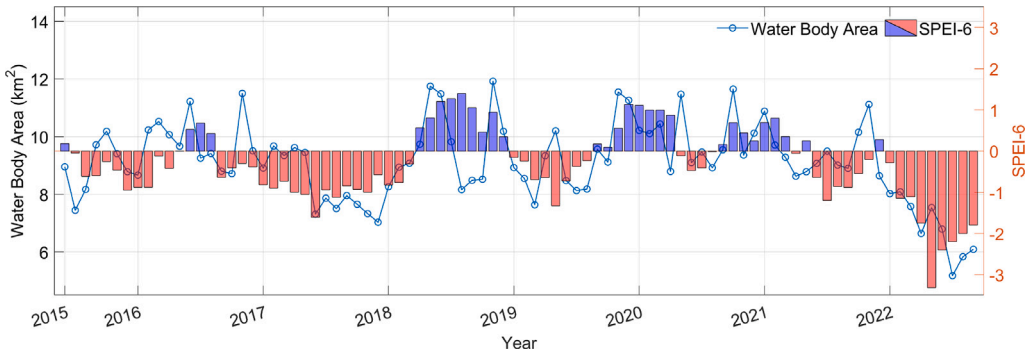

Fig. 12. SAR-based estimates (blue line) are contrasted with the SPEI-6 time series. Note that the red (blue) bars indicate negative (positive) SPEI values. (For interpretation of the references to color in this figure legend, the reader is referred to the web version of this article.)

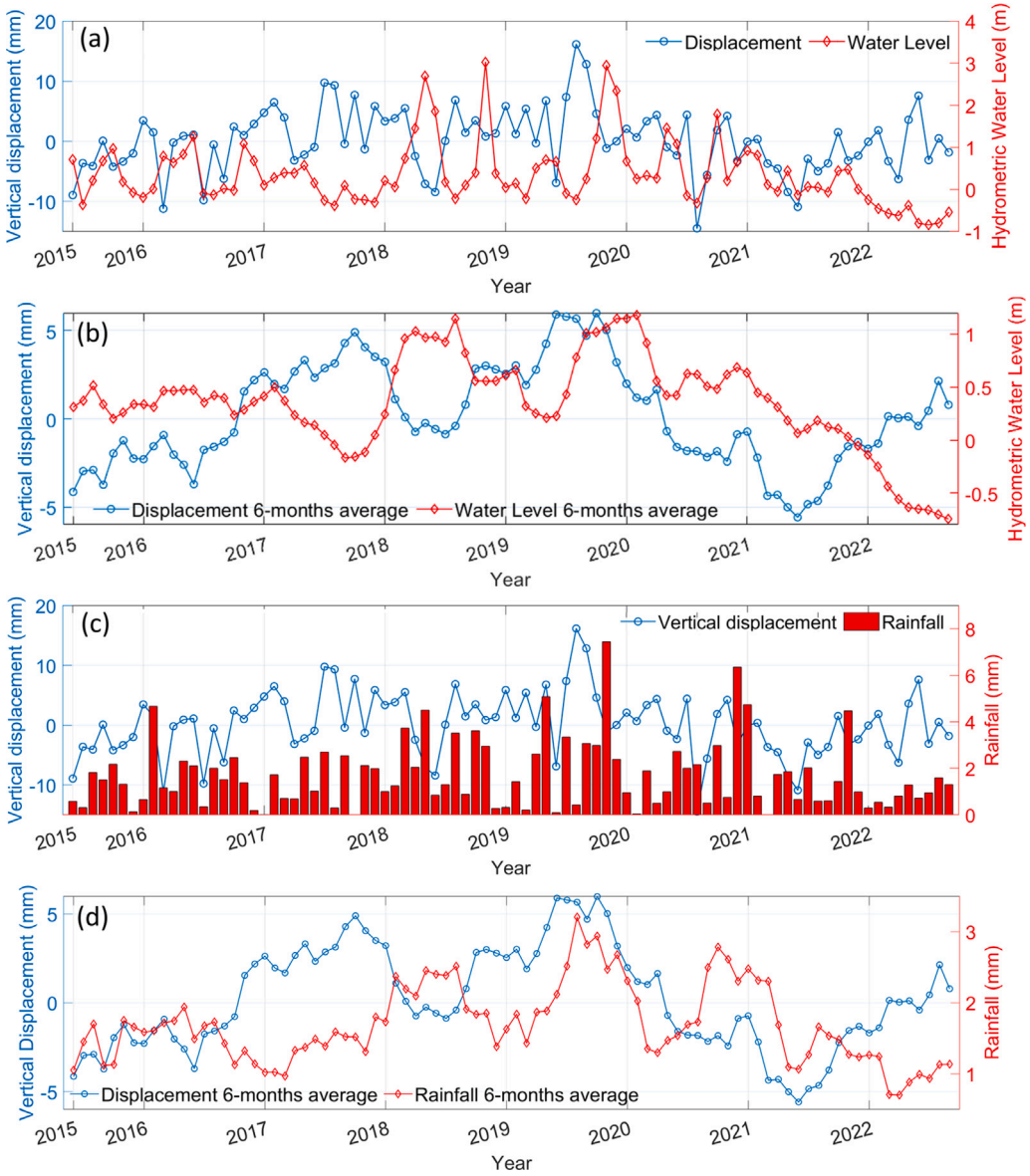

Fig. 13. InSAR-based vertical displacement is contrasted with hydrometric water level (a, b) and rainfall (c, d) data. Both are represented as monthly values (a, c) and 6-month moving averages (b, d).

CRediT authorship contribution statement

Emanuele Ferrentino: Writing – review & editing, Writing – original draft, Visualization, Validation, Supervision, Software, Resources, Methodology, Investigation, Formal analysis, Data curation, Conceptualization. **Marco Polcari:** Writing – review & editing, Writing – original draft, Visualization, Validation, Supervision, Software, Resources, Methodology, Investigation, Formal analysis, Data curation, Conceptualization. **Francesca Silverii:** Writing – review & editing, Writing – original draft, Visualization, Validation, Supervision, Software, Resources, Methodology, Investigation, Formal analysis, Data curation, Conceptualization. **Christian Bignami:** Writing – review & editing, Writing – original draft, Visualization, Resources, Project administration, Methodology, Funding acquisition, Formal analysis, Data curation, Conceptualization. **Ferdinando Nunziata:** Writing – review & editing, Writing – original draft, Visualization, Supervision, Resources, Methodology, Investigation, Formal analysis, Data curation, Conceptualization. **Salvatore Stramondo:** Supervision, Project administration, Investigation, Funding acquisition, Formal analysis. **Maurizio Migliaccio:** Supervision, Project administration, Investigation, Funding acquisition, Formal analysis.

Declaration of competing interest

The authors declare the following financial interests/personal relationships which may be considered as potential competing interests: Emanuele Ferrentino reports was provided by National Institute of Geophysics and Volcanology. If there are other authors, they declare that they have no known competing financial interests or personal relationships that could have appeared to influence the work reported in this paper.

Data availability

Data will be made available on request.

References

Ansari, H., De Zan, F., Parizzi, A., 2021. Study of systematic bias in measuring surface deformation with SAR interferometry. IEEE Trans. Geosci. Remote Sens. 59 (2), 1285–1301. http://dx.doi.org/10.1109/TGRS.2020.3003421.

Antolini, G., Auteri, L., Pavan, V., Tomei, F., Tomozeiu, R., Marletto, V., 2016. A daily high-resolution gridded climatic data set for Emilia-Romagna, Italy, during 1961–2010. Int. J. Climatol. 36 (4), 1970–1986. http://dx.doi.org/10.1002/joc.4473.

Baldi, P., Casula, G., Cenni, N., Loddo, F., Pesci, A., 2009. GPS-based monitoring of land subsidence in the Po Plain (Northern Italy). Earth Planet. Sci. Lett. 288 (1), 204–212. http://dx.doi.org/10.1016/j.epsl.2009.09.023.

Baronetti, A., González-Hidalgo, J.C., Vicente-Serrano, S.M., Acquaotta, F., Fratianni, S., 2020. A weekly spatio-temporal distribution of drought events over the Po Plain (North Italy) in the last five decades. Int. J. Climatol. 40 (10), 4463–4476. http://dx.doi.org/10.1002/joc.6467.

Béjar-Pizarro, M., Ezquerro, P., Herrera, G., Tomás, R., Guardiola-Albert, C., Ruiz Hernández, J.M., Fernández Merodo, J.A., Marchamalo, M., Martínez, R., 2017. Mapping groundwater level and aquifer storage variations from InSAR measurements in the Madrid aquifer, Central Spain. J. Hydrol. 547, 678–689. http://dx.doi.org/10.1016/j.jhydrol.2017.02.011.

Bell, J.W., Amelung, F., Ferretti, A., Bianchi, M., Novali, F., 2008. Permanent scatterer InSAR reveals seasonal and long-term aquifer-system response to groundwater pumping and artificial recharge. Water Resour. Res. 44 (2), http://dx.doi.org/10.1029/2007WR006152.

Berardino, P., Fornaro, G., Lanari, R., Sansosti, E., 2002. A new algorithm for surface deformation monitoring based on small baseline differential SAR interferograms. IEEE Trans. Geosci. Remote Sens. 40 (11), 2375–2383. http://dx.doi.org/10.1109/TGRS.2002.803792.

Bodini, A., Ricci, A., Viaroli, P., 2000. A multimethodological approach for the sustainable management of perifluvial wetlands of the Po River (Italy). Environ. Manag. 26 (1), 59–72. http://dx.doi.org/10.1007/s002670010071.

Bonaldo, D., Bellafiore, D., Ferrarin, C., Ferretti, R., Ricchi, A., Sangelantoni, L., Vitelletti, M.L., 2022. The summer 2022 drought: a taste of future climate for the Po valley (Italy)? Reg. Environ. Change 23 (1), 1. http://dx.doi.org/10.1007/s10113-022-02004-z.

Cavalié, O., Doin, M.-P., Lasserre, C., Briole, P., 2007. Ground motion measurement in the Lake Mead area, Nevada, by differential synthetic aperture radar interferometry time series analysis: Probing the lithosphere rheological structure. J. Geophys. Res.: Solid Earth 112 (B3), http://dx.doi.org/10.1029/2006JB004344.

Chaussard, E., Bürgmann, R., Shirzaei, M., Fielding, E.J., Baker, B., 2014. Predictability of hydraulic head changes and characterization of aquifer-system and fault properties from InSAR-derived ground deformation. J. Geophys. Res.: Solid Earth 119 (8), 6572–6590. http://dx.doi.org/10.1002/2014JB011266.

Clifford, C., 2022. Italy has declared a state of emergency because of drought: "there is no doubt that climate change is having an effect," the prime minister said. URL https://www.cnbc.com/2022/07/05/italy-declared-a-state-of-emergency-because-of-drought-in-the-po-river.html.

Costantini, M., 1998. A novel phase unwrapping method based on network programming. IEEE Trans. Geosci. Remote Sens. 36 (3), 813–821. http://dx.doi.org/10.1109/36.673674.

Crosetto, M., Monserrat, O., Cuevas-González, M., Devanthéry, N., Crippa, B., 2016. Persistent scatterer interferometry: A review. ISPRS J. Photogramm. Remote Sens. 115, 78–89. http://dx.doi.org/10.1016/j.isprsjprs.2015.10.011, URL https://www.sciencedirect.com/science/article/pii/S0924271615002415, Theme issue 'State-of-the-art in photogrammetry, remote sensing and spatial information science'.

Damilano, S., 2022. Po Valley Farmers Living through Italy's worst drought for 70 years. URL https://www.euronews.com/green/2022/07/01/po-valley-farmers-living-through-italys-worst-drought-for-70-years.

Darvishi, M., Destouni, G., Aminjafari, S., Jaramillo, F., 2021. Multi-sensor InSAR assessment of ground deformations around Lake Mead and its relation to water level changes. Remote Sens. 13 (3), http://dx.doi.org/10.3390/rs13030406, URL https://www.mdpi.com/2072-4292/13/3/406.

De Zan, F., Parizzi, A., Prats-Iraola, P., López-Dekker, P., 2014. A SAR interferometric model for soil moisture. IEEE Trans. Geosci. Remote Sens. 52 (1), 418–425. http://dx.doi.org/10.1109/TGRS.2013.2241069.

Ding, X., Li, X., 2011. Monitoring of the water-area variations of Lake Dongting in China with ENVISAT ASAR images. Int. J. Appl. Earth Obs. Geoinf. 13 (6), 894–901. http://dx.doi.org/10.1016/j.jag.2011.06.009.

Doin, M.-P., Twardzik, C., Ducret, G., Lasserre, C., Guillaso, S., Jianbao, S., 2015. InSAR measurement of the deformation around Siling Co Lake: Inferences on the lower crust viscosity in central Tibet. J. Geophys. Res.: Solid Earth 120 (7), 5290–5310. http://dx.doi.org/10.1002/2014JB011768.

Ferrentino, E., Nunziata, F., Buono, A., Urciuoli, A., Migliaccio, M., 2020. Multipolarization time series of Sentinel-1 SAR imagery to analyze variations of reservoirs' water body. IEEE J. Sel. Top. Appl. Earth Obs. Remote Sens. 13, 840–846. http://dx.doi.org/10.1109/JSTARS.2019.2961563.

Ferretti, A., Prati, C., Rocca, F., 2001. Permanent scatterers in SAR interferometry. IEEE Trans. Geosci. Remote Sens. 39 (1), 8–20. http://dx.doi.org/10.1109/36.898661.

Gahalaut, V., Yadav, R.K., Sreejith, K., Gahalaut, K., Bürgmann, R., Agrawal, R., Sati, S., Bansal, A., 2017. InSAR and GPS measurements of crustal deformation due to seasonal loading of Tehri reservoir in Garhwal Himalaya, India. Geophys. J. Int. 209 (1), 425–433. http://dx.doi.org/10.1093/gji/ggx015.

Goldstein, R.M., Werner, C.L., 1998. Radar interferogram filtering for geophysical applications. Geophys. Res. Lett. 25 (21), 4035–4038. http://dx.doi.org/10.1029/1998GL900033.

Li, J., Wang, S., 2015. An automatic method for mapping inland surface waterbodies with Radarsat-2 imagery. Int. J. Remote Sens. 36 (5), 1367–1384. http://dx.doi.org/10.1080/01431161.2015.1009653.

Li, J., Wang, S., Michel, C., Russell, H.A., 2020. Surface deformation observed by InSAR shows connections with water storage change in Southern Ontario. J. Hydrol.: Reg. Stud. 27, 100661. http://dx.doi.org/10.1016/j.ejrh.2019.100661.

Masetti, M., Pettinato, S., Nghiem, S.V., Paloscia, S., Pedretti, D., Santi, E., 2018. Combining COSMO-SkyMed satellites data and numerical modeling for the dynamic management of artificial recharge basins. J. Hydrol. 567, 41–50. http://dx.doi.org/10.1016/j.jhydrol.2018.09.067.

Massonnet, D., Rossi, M., Carmona, C., Adragna, F., Peltzer, G., Feigl, K., Rabaute, T., 1993. The displacement field of the Landers earthquake mapped by radar interferometry. Nature 364 (6433), 138–142. http://dx.doi.org/10.1038/364138a0.

McFeeters, S.K., 1996. The use of the Normalized Difference Water Index (NDWI) in the delineation of open water features. Int. J. Remote Sens. 17 (7), 1425–1432. http://dx.doi.org/10.1080/01431169608948714.

Mira, N.C., Catalão, J., Nico, G., 2024. On the mitigation of phase bias in SAR interferometry applications: A new model based on NDWI. IEEE J. Sel. Top. Appl. Earth Obs. Remote Sens. 17, 3850–3859. http://dx.doi.org/10.1109/JSTARS.2024.3357699.

Mira, N.C., Catalão, J., Nico, G., Mateus, P., 2022. Soil moisture estimation using atmospherically corrected C-band insar data. IEEE Trans. Geosci. Remote Sens. 60, 1–9. http://dx.doi.org/10.1109/TGRS.2021.3109450.

Montanari, A., Nguyen, H., Rubinetti, S., Ceola, S., Galelli, S., Rubino, A., Zanchettin, D., 2023. Why the 2022 Po River drought is the worst in the past two centuries. Sci. Adv. 9 (32), eadg8304. http://dx.doi.org/10.1126/sciadv.adg8304.

Musolino, D., Vezzani, C., Massarutto, A., 2018. Drought management in the Po River basin, Italy. In: Drought. John Wiley & Sons, Ltd, pp. 201–215. http://dx.doi.org/10.1002/9781119017073.ch11.

Pintori, F., Serpelloni, E., 2024. Drought-induced vertical displacements and water loss in the po river basin (northern Italy) from GNSS measurements. Earth Space Sci. 11 (3), http://dx.doi.org/10.1029/2023EA003326, e2023EA003326.

Pipitone, C., Maltese, A., Dardanelli, G., Lo Brutto, M., La Loggia, G., 2018. Monitoring water surface and level of a reservoir using different remote sensing approaches and comparison with dam displacements evaluated via GNSS. Remote Sens. 10 (1), http://dx.doi.org/10.3390/rs10010071.

Polcari, M., Albano, M., Montuori, A., Bignami, C., Tolomei, C., Pezzo, G., Falcone, S., La Piana, C., Doumaz, F., Salvi, S., Stramondo, S., 2018. InSAR monitoring of Italian coastline revealing natural and anthropogenic ground deformation phenomena and future perspectives. Sustainability 10 (9), http://dx.doi.org/10.3390/su10093152.

Polcari, M., Albano, M., Saroli, M., Tolomei, C., Lancia, M., Moro, M., Stramondo, S., 2014. Subsidence detected by multi-pass differential SAR interferometry in the Cassino Plain (Central Italy): Joint effect of geological and anthropogenic factors? Remote Sens. 6 (10), 9676–9690. http://dx.doi.org/10.3390/rs6109676.

Raman, M., Aggarwal, H., 2009. Study and comparison of various image edge detection techniques. Int. J. Image Process. 3.

Roeloffs, E.A., 2001. Creep rate changes at Parkfield, California 1966–1999: Seasonal, precipitation induced, and tectonic. J. Geophys. Res.: Solid Earth 106 (B8), 16525–16547. http://dx.doi.org/10.1029/2001JB000352.

Saleh, M., Masson, F., Mohamed, A.-M.S., Boy, J.-P., Abou-Aly, N., Rayan, A., 2018. Recent ground deformation around lake Nasser using GPS and InSAR, Aswan, Egypt. Tectonophysics 744, 310–321. http://dx.doi.org/10.1016/j.tecto.2018.07.005, URL https://www.sciencedirect.com/science/article/pii/S0040195118302488.

Serpelloni, E., Faccenna, C., Spada, G., Dong, D., Williams, S.D.P., 2013. Vertical GPS ground motion rates in the Euro-Mediterranean region: New evidence of velocity gradients at different spatial scales along the Nubia-Eurasia plate boundary. J. Geophys. Res.: Solid Earth 118 (11), 6003–6024. http://dx.doi.org/10.1002/2013JB010102.

Slovenian Environment Agency, & Central Institution for Meteorology and Geodynamics, 2022. Standardised Precipitation-Evapotranspiration Index - ERA5_QM SPEI-1 (Version 1.0) [Data set]. Eurac Research. http://dx.doi.org/10.48784/166e51ee-534a-11ec-9143-02000a08f41d.

Stacy, E., 1962. A generalization of the Gamma distribution. Ann. Math. Stat. 33 (3), 1187–1192.

Stramondo, S., Bozzano, F., Marra, F., Wegmuller, U., Cinti, F., Moro, M., Saroli, M., 2008. Subsidence induced by urbanisation in the city of Rome detected by advanced InSAR technique and geotechnical investigations. Remote Sens. Environ. 112 (6), 3160–3172. http://dx.doi.org/10.1016/j.rse.2008.03.008.

Vicente-Serrano, S.M., Beguería, S., López-Moreno, J.I., 2010. A multiscalar drought index sensitive to global warming: The standardized precipitation evapotranspiration index. J. Clim. 23 (7), 1696–1718. http://dx.doi.org/10.1175/2009JCLI2909.1.

Vitagliano, E., Riccardi, U., Piegari, E., Boy, J.-P., Di Maio, R., 2020. Multi-component and multi-source approach for studying land subsidence in deltas. Remote Sens. 12 (9), http://dx.doi.org/10.3390/rs12091465, URL https://www.mdpi.com/2072-4292/12/9/1465.

Wang, H., Wright, T.J., Yu, Y., Lin, H., Jiang, L., Li, C., Qiu, G., 2012. InSAR reveals coastal subsidence in the Pearl River Delta, China. Geophys. J. Int. 191 (3), 1119–1128. http://dx.doi.org/10.1111/j.1365-246X.2012.05687.x.

Wegmuller, U., 1997. Gamma SAR processor and interferometry software. In: 3rd ERS Symposium, Florence, Italy, March 1997.

Werner, C.L., Wegmüller, U., Strozzi, T., 2012. Deformation time-series of the Lost-Hills oil field using a multi-baseline interferometric SAR inversion algorithm with finite difference smoothing constraints. In: AGU Fall Meeting Abstracts. 2012, pp. G43A–0910.

White, A.M., Gardner, W.P., Borsa, A.A., Argus, D.F., Martens, H.R., 2022. A review of GNSS/GPS in hydrogeodesy: Hydrologic loading applications and their implications for water resource research. Water Resour. Res. 58 (7), http://dx.doi.org/10.1029/2022WR032078.

Xing, L., Tang, X., Wang, H., Fan, W., Wang, G., 2018. Monitoring monthly surface water dynamics of Dongting Lake using Sentinel-1 data at 10 m. PeerJ 6, http://dx.doi.org/10.7717/peerj.4992.

Yi, Z., Haijun, H., Yanxia, L., Haibo, B., Zehua, Z., Kuifeng, W., Liwen, Y., 2021. Impacts of soft soil compaction and groundwater extraction on subsidence in the Yellow River Delta. Mar. Georesour. Geotechnol. 39 (12), 1497–1504. http://dx.doi.org/10.1080/1064119X.2020.1854909.

Zeng, L., Schmitt, M., Li, L., Zhu, X.X., 2017. Analysing changes of the Poyang Lake water area using Sentinel-1 synthetic aperture radar imagery. Int. J. Remote Sens. 38 (23), 7041–7069. http://dx.doi.org/10.1080/01431161.2017.1370151.

Zhao, W., Amelung, F., Doin, M.-P., Dixon, T.H., Wdowinski, S., Lin, G., 2016. InSAR observations of lake loading at Yangzhuoyong Lake, Tibet: Constraints on crustal elasticity. Earth Planet. Sci. Lett. 449, 240–245. http://dx.doi.org/10.1016/j.epsl.2016.05.044.